Ship detection and tracking from single ocean-bottom seismic and hydroacoustic stations

Alister Trabattoni, Guilhem Barruol, Richard Dréo, Abdel Boudraa

JASA ARTICLE

Ship detection and tracking from single ocean-bottom seismic and hydroacoustic stations

Alister Trabattoni,[1,a,b] Guilhem Barruol,[1,c] Richard Dréo,[1,b] and Abdel Boudraa[2]
[1]*Institut de physique du globe de Paris, Université de Paris Cité, CNRS, F-75005 Paris, France*
[2]*Ecole Navale IRENav/Arts & Métiers ParisTech, BCRM, CC 600, 29240 Brest, France*

ABSTRACT:
We report in this study how ocean-bottom seismometers (OBS) can be used as passive sonars to automatically detect, localize, and track moving acoustic sources at the ocean surface. We developed single-station methods based on direction of arrival and on multi-path interference measurements capable of handling continuous erratic signals emitted by ships. Based on a Bayesian mathematical framework, we developed an azimuthal detector and a radial detector and combined them into a fully automatic tracker. We tested the developed algorithm on seismic and hydroacoustic data recorded in the Indian Ocean by an OBS deployed at 4300 m depth, 200 km west of La Réunion Island. We quantified the performances using archives of commercial-vessel trajectories in the area provided by the Automatic Identification System. Detectors demonstrate capabilities in the detection range up to 100 km from the OBS with azimuthal accuracies of a few degrees and with distance accuracies of a few hundred of meters. We expect the method to be easily transposed to any other kind of sources (such as marine mammals).
 https://doi.org/10.1121/10.0016810
(Received 27 June 2022; revised 2 December 2022; accepted 12 December 2022; published online 17 January 2023)
[Editor: Stan E. Dosso] Pages: 260–273

I. INTRODUCTION

The ocean is an economic asset with high ecological and political stakes, which is continuously crisscrossed by commercial vessels. Most of them are involved in shipping and fishing. Both activities have major impacts on the ocean ecosystems and on fishery resources: overfishing (FAO, 2020), oils, chemical and debris spilling (Zhang *et al.*, 2019), underwater noise pollution (Rako-Gospić and Picciulin, 2019), and collisions with the marine megafauna (Ritter and Panigada, 2019). In response to the decrease in fishery resources and stronger ecological policies, illicit acts such as illegal fishing or "wild" degassing are becoming commonplace. The increase in piracy acts is also endangering the safety of people and property as well as the political stability of certain oceanic regions and their exclusive economic zones. Along the coasts, visual or radar surveillance can be set up by local authorities. In the open sea and uninhabited areas, these solutions are more challenging and unrealistic on a large scale. Global surveillance of high seas mainly relies on satellite imagery technologies, which are highly dependent on weather conditions. Over the last decade, the development of satellite Automatic Identification System (AIS) and the obligation for ships over 300 gross tonnages to embark on an AIS transmitter theoretically make it possible to know the position of any ship at any time. Unfortunately, this surveillance is limited to large vessels and the falsification (e.g., by simulating a transmitter failure) of AIS data can easily mislead this surveillance system. In this context, the development of other low-cost passive modalities of observation and monitoring of the oceans seems important.

The geophysical research community is an important player in the instrumentation of the ocean floor. In particular, many ocean-bottom seismometers (OBSs) are temporarily deployed each year as submarine networks with scientific objectives focused on seismic hazards (induced by landslides, volcanoes, faults, …), on deep earth imaging, and the study of the dynamics of our planet. Those instruments measure the seafloor vibrations, hence mechanical waves traveling into the solid earth, but also water pressure variations, hence acoustic waves travelling through the ocean. They are therefore suitable for recording earthquakes but also ship noise, marine mammal calls, storms and sea ice activities, etc. The detection and localization of whales using OBSs have been extensively studied (Wilcock, 2012; Harris *et al.*, 2013; Weirathmueller *et al.*, 2017; Bouffaut *et al.*, 2018; Dréo *et al.*, 2019; Wilcock and Hilmo, 2021). Unfortunately, methods developed for whale calls may not apply to ships that emit continuous and monotonous noise rather than short, impulsive, and frequency-rich acoustical events. If the study of ship noise, using hydrophones is common practice in the underwater acoustic field (e.g., Gervaise *et al.*, 2012; Ferguson *et al.*, 2018), performing underwater passive tracking using a pressure sensor co-located with a three-dimensional (3D) velocity sensor (or in other terms, an acoustic vector sensor, AVS) is a new rising field of research (Stinco *et al.*, 2021a; Stinco *et al.*, 2021b; Dréo

[a]Electronic mail: alister.trabattoni@gmail.com
[b]Also at: Ecole Navale IRENav/Arts & Métiers ParisTech, BCRM, CC 600, 29240 Brest, France.
[c]Also at: Institut des Géosciences de l'Environnement (IGE), University of Grenoble Alpes, CNRS, IRD, Grenoble INP, 38000 Grenoble, France.

https://doi.org/10.1121/10.0016810

et al., 2022). To our knowledge, the use of OBSs as AVSs to track ships has yet not been done and represents the focus of the present work. To achieve this, we propose a Bayesian framework for detection and tracking adapted to underwater passive monitoring at low frequency with AVSs. This work is the continuation of a previous study (Trabattoni *et al.*, 2019) in which ship noise was used to derive the accurate orientations and localizations of OBSs from AIS-derived ship positions. Here, we approach the inverse problem: how to retrieve blindly the trajectory of a ship from hydro-seismological records of a single station lying on the ocean floor. In the following, we will first describe the data we worked on, before describing the methodology and its application to an OBS deployed in the Southwest (SW) Indian Ocean.

II. EXPERIMENT AND OBSERVABLES

To develop and validate methods, we used hydro-acoustic and seismological records from the Réunion Hotspot and Upper Mantle–Réunions Unterer Mantel (RHUM-RUM) experiment. The objective of this experiment was to investigate the presence or absence of a mantle plume beneath the Réunion hotspot and to image the upper and lower mantle structures beneath the SW Indian Ocean (Barruol and Sigloch, 2013; Mazzullo *et al.*, 2017; Scholz *et al.*, 2018; Barruol *et al.*, 2019; Hable *et al.*, 2019; Tsekhmistrenko *et al.*, 2021). A total of 57 OBSs have been deployed for 13 months, from October 2012 to December 2013 at depths ranging from 2500 to 5000 m and covering a wide area of roughly $2000 \times 2000\,\mathrm{km}^2$ around La Réunion Island, between Madagascar and the neighboring South-West and Central Indian oceanic ridges (Fig. 1). Technical details on the deployment, performance, and data availability from this ocean-bottom experiment can be found in Stähler *et al.* (2016). Interestingly, this deployment was partially located beneath the marine commercial route linking South Atlantic and South-East Asia (Cape of Good Hope to the Strait of Malacca) involving high marine traffic above some parts of the RHUM-RUM OBS network. To assess the accuracy of the detection and localization methods, archives of ship positions were acquired (Fig. 1). Two AIS datasets were used: (i) A satellite-based dataset (S-AIS) purchased from Collecte Localisation Satellites (CLS). This dataset covered the whole experiment both in time and space. It provides ship status every hour on average, but gaps of three or more hours are common in the database. Because of long-duration gaps, ship positioning can be inaccurate when interpolating positions between successive logs. (ii) A terrestrial-based AIS dataset (T-AIS) completes this first satellite dataset, kindly obtained as a free sample from MarineTraffic (https://www.marinetraffic.com). This second dataset provides a dense coverage limited to a small area around La Réunion Island and covering only the month of November 2012, which is the first month where all seismological stations were deployed and operational.

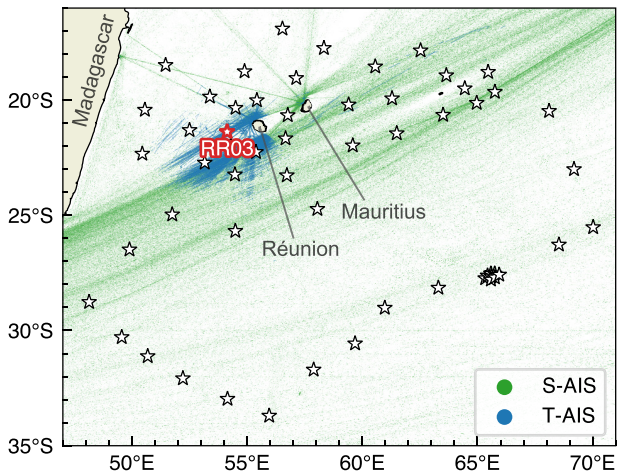

FIG. 1. (Color online) RHUM-RUM experiment and its AIS coverage. This experiment allowed the deployment of 57 OBSs (stars) around La Réunion Island and on the neighboring mid-ocean ridges from October 2012 to November 2013. Two AIS datasets have been used in the present study for validating detections from seismo-hydroacoustic data. A satellite-based dataset (S-AIS, in green) covers the whole spatial and temporal extents of the experiment but with a poor time rate of ship positions. A terrestrial based dataset (T-AIS, in blue) covers the month of November 2012 and a small spatial extent in the vicinity of La Réunion but at a much higher time rate. The station RR03 used throughout this article (red star) was located in an area of good T-AIS coverage and flat bathymetry.

Because of the T-AIS spatial coverage and restrictions due to partial failure of some seismological stations (see Stähler *et al.*, 2016), this study focuses on data recorded by the station RR03 (Fig. 1). This station is located at 4340 m depth, about 200 km west of Réunion island, onto a flat ocean floor covered by sediments, which simplifies the modeling of wave propagation. The localization and orientation of the station were retrieved from Trabattoni *et al.* (2019). We chose the month of November 2012 with its high accuracy T-AIS to calibrate the propagation model required for distance estimation (see later Sec. III C). The month of November is particularly interesting in this area because no whale vocalization "polluted" the recordings (Dréo *et al.*, 2019), allowing for cleaner ship signals and hence more precise calibration procedures. To further test the developed methods, this study then focuses on the six-day period of May 21–27, 2013 (Fig. 2), covering typical sources that can be observed by OBSs in that region: (i) Ships that can be easily recognized by their several hour-long acoustic signatures, made of different monotonic tones and their harmonics which frequencies are linked to the rotating rate of engines and/or the number of blades of the propeller. (ii) Whale calls that are stereotyped repeated impulsive acoustical events, the shape of which, in a time-frequency spectrogram representation, allows us to identify the species. The test period occurs at the beginning of whale migration in the area (Samaran *et al.*, 2013). When numerous individuals evolve in the vicinity, the superposition of their conversations generates a cheerful hubbub called whale chorus. (iii) Seismic events that are isolated short broadband signals, the central frequency of whose depends, among others, on the distance of the source and its power. (iv) Ocean bottom currents that may mechanically interact with the OBS structure, in particular for some OBS designs, where the presence of a head buoy used for easy recovery at

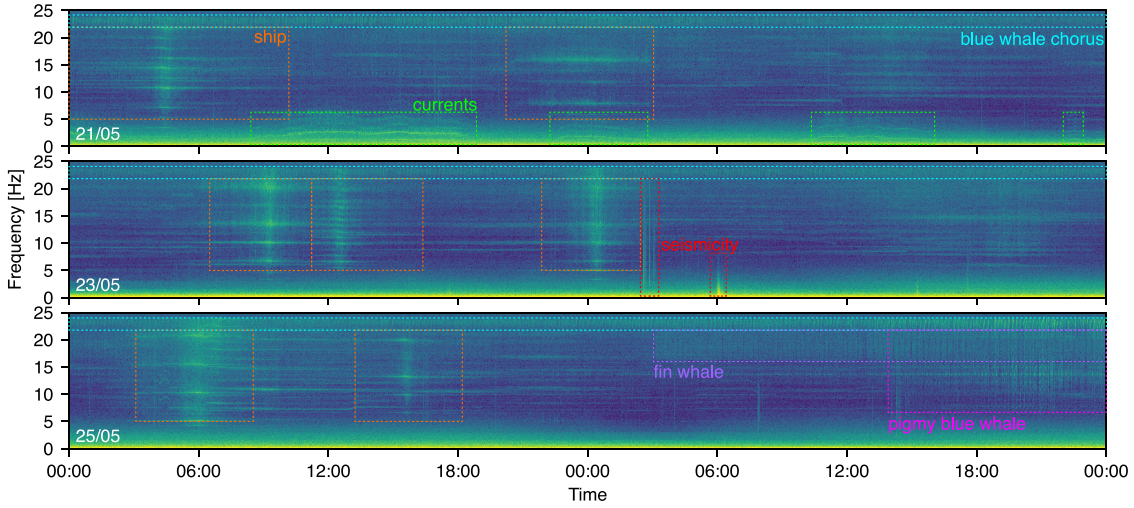

FIG. 2. (Color online) Spectrogram between 0 and 25 Hz illustrating the ocean soundscape recorded by the station RR03 during the six-day long test period of May 21 to 27, 2013. This period corresponds to the beginning of the baleen whale's migration in the area close to La Réunion Island. Most observed sources can be seen on this plot and are underlined by colored dotted-line boxes: ships (orange), baleen whales (blue, purple, and pink, for blue whales, fin whales and pigmy blue whales, respectively), seismicity (red), and, in the case of this OBS, the swinging and oscillation of the head buoy and rope induced by bottom water currents (green).

surfacing and connected to the OBS structure with a rope generates a water current induced noise on the recordings (Stähler *et al.*, 2018; Essing *et al.*, 2021).

III. METHODOLOGY

The objective of this study is to propose a methodology capable of reconstructing automatically trajectories of ships passing nearby an isolated OBS of known orientation and localization, without any *a priori* knowledge of the ship's presence and position. This is a complex problem that requires, in the general case, to solve multiple challenging subproblems: (i) wave propagation in a 3D environment; (ii) advanced signal processing and statistical methods to treat the four components of OBSs in the case of continuous seismo-acoustic signals; (iii) multi-object tracking. In this study, three hypotheses were made to reduce this complexity by taking advantage of some particularity representing most of the encountered scenarios: (a) Physical properties of the ocean were considered horizontally invariant. This hypothesis is satisfactory for stations located in sedimentary basins (such as RR03) where a simple one-dimensional (1D) vertical sound speed model with constant ocean depth suffices to predict wave propagation with great accuracy. (b) At most one ship was considered to be present. Even if multiple ships could be observed simultaneously (see, for instance, Fig. 2 on May 25, 2013), those situations are minoritarian and methods were not designed for this use case. (c) Ship trajectories were supposed to be rectilinear and at constant speed. This is a good approximation for merchant ships which represent most of the ships crossing around RR03 but does not apply, for example, to fishing boats that may have more erratic trajectories in both azimuths and speeds.

To reconstruct ship trajectories, different intermediate steps will be presented. First, a detection and localization approach will be constructed independently for the azimuth and the range estimation. Those two measurements rely on distinctive features of ship noise and cannot be treated simultaneously. Then, combining the azimuth and range algorithms, a temporal segmentation algorithm will be constructed to discern non overlapping time segments where the reconstruction of the trajectory of a particular ship will then be computed by fitting a rectilinear constant speed trajectory. For a more in-depth understanding of the following proposed methods, the developed codes used in this article can be found as part of an open-source python package named *obsea* (see Acknowledgments).

A. Bayesian approach

In this study, a Bayesian approach is used to analyze the OBS recordings. This solid mathematical framework exploits the information conveyed by OBSs, based on statistical *a priori* knowledge derived from physical considerations. Methods and notations developed here were inspired by Stone *et al.* (2014) and will be briefly introduced here.

The objective is to estimate the most probable state s (position, speed, etc.) of at most one ship in some surveillance domain S (or state space). The case where no ship is present is referred as the null space state, noted $\varnothing$. The probability of presence of a target regardless of its state is noted $P(\mathbb{1})$. Since either hypothesis $\varnothing$ or $\mathbb{1}$ occurs it comes

$$P(\varnothing) + \int_S P(s)\mathrm{d}s = P(\varnothing) + P(\mathbb{1}) = 1. \tag{1}$$

The detection process consists in estimating the posterior (superscript $+$) probability $P^+(s|y)$ of the state s given some observation y. Bayes' theorem allows us to rewrite this probability as

$$P^+(s|y) = \frac{L(y|s)P^-(s)}{L(y|\varnothing)P^-(\varnothing) + \int_S L(y|s)P^-(s)\mathrm{d}s}. \tag{2}$$

https://doi.org/10.1121/10.0016810

It is indeed easier to compute the likelihood $L(y|s)$ which consists of modeling the expected observation y from a given state s. The *a priori* knowledge on the state s is taken into account in the prior (superscript $-$) probability $P^-(s)$. The right term of the equation is divided by a normalization term that is generally not directly computed but instead chosen to ensure that the posterior distribution integrates to one.

The problem can be further simplified by working with likelihood and probability ratios between the presence and the absence cases,

$$\mathcal{L}(y|s) = \frac{L(y|s)}{L(y|\varnothing)}, \quad \mathcal{P}^+(s|y) = \frac{P^+(s|y)}{P^+(\varnothing|y)}, \quad \mathcal{P}^-(s) = \frac{P^-(s)}{P^-(\varnothing)}. \tag{3}$$

Using those likelihood and probability relations, Eq. (2) simplifies into

$$\mathcal{P}^+(s|y) = \mathcal{L}(y|s)\mathcal{P}^-(s). \tag{4}$$

The rules that will be used to decide if a target is present is to consider $\mathcal{P}^+(\mathbb{1}|y) = \int_S \mathcal{P}^+(s|y)\mathrm{d}s > 1$, i.e., when $P^+(\mathbb{1}|y) > P^+(\varnothing|y)$. This rule corresponds to the special case of the *ideal receiver* in Bayes' risk evaluation (Poor, 1994). It minimizes the average number of classification errors (false positives and false negatives). Other rules can be chosen, if, for example, false positives are more problematic than false negatives.

At this stage, the state s and observation y have been taken in the broadest sense. The state s can represent any set of parameters describing, even partially, the ship trajectory; the observation y can represent any set of measurements made on the OBS traces.

B. Azimuthal detection and localization

The azimuth estimation is enabled by the three-component seismological sensor embedded into the OBS. The seismometer allows us to measure the direction of arrival (both horizontally and vertically) of incoming waves by comparing the amplitude of the three different components (e.g., Fontaine *et al.*, 2009). This measurement is accurate only when the signal-to-noise ratio (SNR) is high enough, otherwise, the measured angle can be corrupted by background noise or by secondary source signals. Using the Short-Time Fourier Transform (STFT), signals of the four components (three seismic and one hydroacoustic) are first transformed into time-frequency representations $S_p(t,f)$ and $\boldsymbol{S_v}(t,f) = [S_{v_N}(t,f), S_{v_E}(t,f), S_{v_D}(t,f)]$ (pressure and 3D particle motion in the North, East, and Down reference coordinate system). Time-frequency representations are reconstructed with the fast Fourier transform (FFT) length set to 512 samples (i.e., ∼10 s at 50 Hz) with an overlap of 50% and a Hann tapering function.

In the frequency domain, ship noise consists of a series of tones and harmonics of high intensity where the ship signal clearly predominates on background noise and generally does not overlap with other sources (Fig. 2). To compute the incident angle, the active acoustic intensity $\boldsymbol{I}$ was computed (Mann *et al.*, 1987) as follows:

$$\boldsymbol{I}(t,f) = \frac{1}{2}\mathrm{Re}\left(S_p{}^*(t,f)\cdot \boldsymbol{S_v}(t,f)\right). \tag{5}$$

The active acoustic intensity is a vector pointing toward the direction of propagation of the energy. The azimuth was computed by measuring the horizontal angle of the active acoustic intensity. Computing the azimuth for each time-frequency bin gives a time-frequency representation called azigram (Thode *et al.*, 2019) that was already introduced in a previous study to retrieve the OBS orientation at depth from the AIS-known ship location (Trabattoni *et al.*, 2019). This will be used as our azimuthal observation noted y_α (where the subscript α refers to azimuth) which is computed from the east and north component of the acoustic intensity as

$$y_\alpha(t,f) = \arctan(I_\mathrm{E}(t,f), I_\mathrm{N}(t,f)). \tag{6}$$

To illustrate this concept, the azigram computed for the passage of a ship passing near RR03 on November 27, 2012, is shown in Fig. 3(a). The azimuthal variation of the ship is

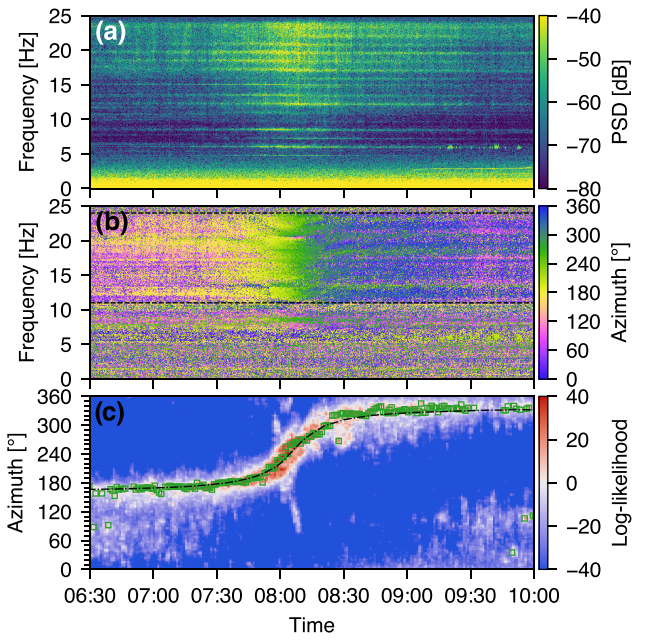

FIG. 3. (Color online) Azimuthal detection at station RR03. (a) Spectrogram of the vessel BUXCONTACT passage (MMSI: 211 739 000 206 × 28 m container ship) on November 27, 2012. The energy of the narrow-band tonal features of the ship noise reaches high values of SNR. (b) Azigram signature of the passing vessel. The azimuthal variation of the ship is measured between 11 and 24 Hz (horizontal dashed lines) and evolves continuously from ∼180° (yellow) to ∼360° (blue). Note that the background noise is not completely isotropic in that example and is directed toward ∼90° (pink). When the ship is at a large distance, the azimuth of the ship can only be observed on narrow frequency bands. (c) Log-likelihood ratio of the presence of a ship at a given time and azimuth. When the Bayes criterion is met, the azimuth of the ship is estimated as the maximum of the log-likelihood ratio (green squares). The detections closely follow the expected azimuths predicted by the T-AIS dataset (black dashed line). A limited number of false negatives are observed when the ship is at large distance and might be due to other sources in the vicinity.

clearly visible by the color variation with time [Fig. 3(b)], especially in specific narrow band regions where ship noise predominates.

The detection was performed on small sliding time windows of $T = 3$ min with a time step of 1 min. The size of those windows was chosen as long as possible to improve detection, and short enough so that ship azimuth (and later on, ship radial speed) can be considered constant. For each time window, the values of the azigram are expected to follow different statistical laws whether ship signal or background noise dominates.

Where ship signal dominates, the measured azimuth was modeled to vary according to a Wrapped Cauchy distribution $\mathcal{WC}(\alpha, R)$ (Mardia and Jupp, 1999). Its probability density function is given by

$$\mathcal{WC}(y_\alpha|\alpha, R) = \frac{1}{2\pi}\frac{1-R^2}{1-2R\cos(y_\alpha-\alpha)+R^2}. \tag{7}$$

Here, the peak position α is the true ship direction and the mean resultant length R describes how much we expect the ship signal to be focalized around the true direction of the ship (from 0 being the uniform distribution and 1 the Dirac distribution). The circular variance varies with the SNR. Its value was set to $R = 0.99$ which corresponds to a SNR of $+40$ dB (see Appendix B).

Background noise was assumed to be isotropic, and in the time-frequency region where it dominates, it was modeled to follow a uniform law $\mathcal{U}$ over all possible azimuths,

$$U(y_\alpha) = \frac{1}{2\pi}. \tag{8}$$

For the null case $\varnothing$, the background noise dominates. In presence of a vessel, ship noise dominates on a subset of the time-frequency plane. Instead of solving the inherent problem of the ship harmonic structure, tonal features were separately detected at each frequency. Then the marginalized probability of the presence of any tonal feature was computed as the probability of ship presence.

The signal of a tonal feature is expected to continuously dominate at a unique frequency f. The likelihood is given by the product of the expected probability of the observation for each time-frequency bin, assuming that bins are statistically independent. This is not exactly the case as some correlation exists between nearby values in the STFT, yet those effects were neglected for simplicity. Between the presence at direction α case and the null case $\varnothing$ the models only differ for the values at frequency f. Hence only those values eventually need to be taken into account to compute the likelihood *ratio*,

$$\mathcal{L}_\alpha(y_\alpha|t, f, \alpha) = \prod_{|\delta t|<T/2} \frac{\mathcal{WC}(y_\alpha(t+\delta t, f)|\alpha, R)}{\mathcal{U}(y_\alpha(t+\delta t, f))}. \tag{9}$$

The prior probability of the presence of a tonal peak at a frequency f was supposed uniform over a frequency range $[f_{\min}, f_{\max}]$ of 11–24 Hz in our OBS observations. Outside this frequency range, the azigram showed to have poor performance for the station RR03. The prior probability of a ship presence was considered equiprobable with its absence. The prior probability of the ship position was supposed equiprobable on the surveillance area, which translates into uniform azimuthal prior. This gives the following prior probability ratio,

$$\mathcal{P}^-_\alpha(t, f, \alpha) = \begin{cases} \dfrac{1}{(f_{\max}-f_{\min})}\dfrac{1}{2\pi}, & f_{\min} \le f \le f_{\max} \\ 0 & \text{otherwise.} \end{cases} \tag{10}$$

This probability allowed us to compute the marginalize posterior probability over f (where f_s is the Nyquist frequency),

$$\begin{aligned} \mathcal{P}^+_\alpha(t, \alpha|y_\alpha) &= \int_0^{f_s} \mathcal{P}^+_\alpha(t, f, \alpha|y_\alpha) df \\ &= \int_0^{f_s} \mathcal{L}_\alpha(y_\alpha|t, f, \alpha)\mathcal{P}^-_\alpha(t, f, \alpha) df. \end{aligned} \tag{11}$$

This processing was repeated on each sliding window producing a time-azimuth representation of the posterior probability ratio of presence at a given time and azimuth [Fig. 3(c)].

For each time window, the Bayes criterion was used to estimate a ship presence. This was computed as follows:

$$\mathcal{P}^+_\alpha(t, \mathbb{1}|y_\alpha) = \int_0^{2\pi} \mathcal{P}^+_\alpha(t, \alpha|y_\alpha) d\alpha. \tag{12}$$

If $\mathcal{P}^+_\alpha(t, \mathbb{1}|y_\alpha) > 1$ a detection occurs. The given estimated azimuth was obtained finding the maximum *a posteriori* probability (MAP) over α:

$$\hat{\alpha}(t) = \begin{cases} \underset{\alpha}{\text{argmax}}\, \mathcal{P}^+_\alpha(t, \alpha|y_\alpha), & \mathcal{P}^+_\alpha(t, \mathbb{1}|y_\alpha) > 1 \\ \varnothing & \text{otherwise.} \end{cases} \tag{13}$$

To illustrate this azimuthal detector, this processing was applied to the test ship passage (Fig. 3) and detections were compared with the ground truth given by the T-AIS dataset. The azimuthal detector performs very well, with only few false negatives, at distances up to about 100 km in that case. A continuous azimuthal detection is therefore achieved and must be completed by a distance estimator.

C. Radial detection and localization

The multipath propagation of acoustic waves into the ocean involving different numbers of reflections on the ocean floor and surface can be used to constrain the distance between the source (the ship) and the receiver [the OBS, see Fig. 4(a)]. As ship noise is continuous, picking phase arrivals in the time domain is impossible. Instead, the analysis of interferences produced by the multipath propagation can be performed in the frequency domain. More specifically, cepstral analysis was used (Oppenheim and Schafer, 2004; Gao *et al.*, 2014; Trabattoni *et al.*, 2019). This nonlinear processing technique allows us to retrieve the time difference of

https://doi.org/10.1121/10.0016810

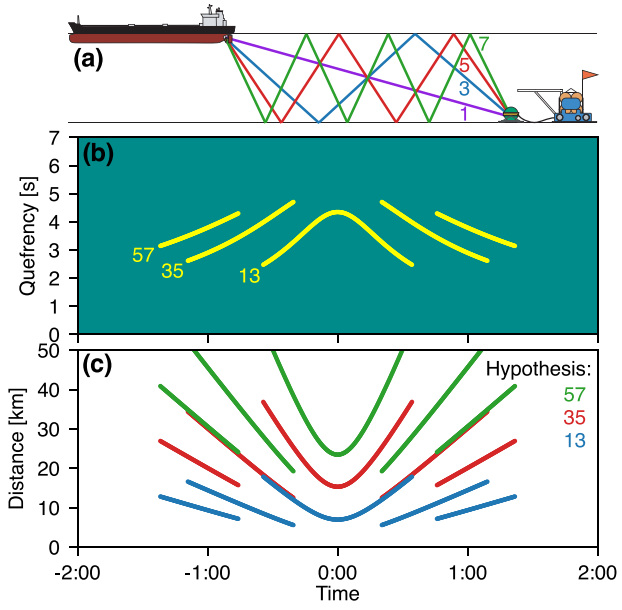

FIG. 4. (Color online) Interference association problem. (a) Acoustic waves emitted by a ship can reach the OBS following several possible acoustical paths, here indicated by the number of vertical crossings of the water column. (b) On the cepstrogram, the interferences between paths can be observed as branches of varying quefrency as the ship transits in the neighborhood of the OBS. (c) To retrieve the distance of the ship from the receiver, hypotheses must be made to link paths between the various branches. In the case of the OBS station RR03, three interferences (13, 35, and 57) are dominantly observed. Each branch can potentially result from one of those three interferences, therefore indicating three potential distances of the ship. The ambiguity can only be solved when several branches are observed at the same time. At those moments, the distance that allows us to conciliate two hypotheses is the only solution. A global approach looking for the only hypothesis allowing for the continuity of the ship distance during the whole ship passage is then necessary.

arrival (TDOA) between different propagation paths. The cepstrogram $C_x(t,\tau)$ is defined as the inverse Fourier transform of the log-spectrogram of the signal $x(t)$ of interest,

$$C_x(t,\tau) = \mathcal{F}^{-1}\Big\{\log\big|S_x(t,f)\big|\Big\}. \tag{14}$$

The cepstrogram allows us to highlight periodicity in the log-spectrogram that can be due either to the harmonic structure of the source or to the multipath propagation interferences [Fig. 4(b)]. Considering that ship noise has a time-invariant harmonic structure whereas multipath interferences evolve with time as the ship moves through space, the cepstrogram can be decomposed as the sum of a source term $C_s(t,\tau)$ and a propagation term $C_g(t,\tau)$ using Singular Value Decomposition (SVD) clutter filtering (Trabattoni *et al.*, 2019; see Appendix A). The cepstrogram is expressed as a function of the time t and the quefrency τ which, in the case of the propagation term, directly transposes into TDOA [Fig. 4(b)]. This processing was applied by chunks of 3 h on the hydrophone component (that better records water waves) and was used as the starting point of the Bayesian analysis as the source radial observation $y_r(t,\tau)$ (where the subscript r refers to radial).

To retrieve the distance of the ship, the measured TDOAs must be associated with the interference involving the right pair of propagation paths. Then, a propagation model can be used to link the TDOA to the source distance. Without any *a priori* knowledge, every measured TDOA can be attributed to several interferences leading to an association problem [Fig. 4(c)]. This problem can only be solved when several TDOAs are measured simultaneously since in that case, only one set of multipaths association hypotheses is possible. A global approach to the problem must be used to retrieve the complete trajectory of the ship and that continuity hypothesis must be used to find the correct solution.

To perform distance detection, a Bayesian approach similar to the one used for the azimuthal detector is developed.

In the absence of source, each time-quefrency bin of the background noise can be closely modeled by zero centered Gaussian processes (see Appendix B). The way the variance $\sigma^2(\tau)$ of the background noise vary with the quefrency τ mainly depends on the window used in the FFT computation. For the Hann window, we observed from Monte Carlo simulations (see Appendix B) that the standard deviation can be very accurately approximated by

$$\sigma(\tau) = (0.625 + 0.2 \times \cos(\pi \times \tau/\tau_s))/\sqrt{N_{\mathrm{FFT}}}. \tag{15}$$

Here, τ_s is the maximal quefrency that is dictated by the size of the window used for FFT computation.

In presence of a ship, we concluded from Monte Carlo simulation (see Appendix B) that interferences produce an additive term $\mu(r,\tau)$ mostly null except at the specific quefrencies linked to the TDOA between the interfering paths that occur when the ship is at distance r [or $r(t)$ when referring to a moving target],

$$y_r(t,\tau) \sim \begin{cases} \mathcal{N}\big(0,\sigma^2(\tau)\big) & \text{if } \varnothing \\ \mathcal{N}\big(\mu(r(t),\tau),\sigma^2(\tau)\big) & \text{otherwise.} \end{cases} \tag{16}$$

The term $\mu(r,\tau)$ was modeled as a sum of Gaussian pulses $\mu_{ij}(r,\tau)$. Each pulse corresponds to the interference produced by the paths crossing, respectively, i and j times the water column. Each pulse has an amplitude $a_{ij}(r)$ that was determined from measurements (see later), a quefrency (or TDOA) $\tau_{ij}(r)$ and phase difference (or PDOA) $\phi_{ij}(r)$ that were determined from a propagation model (see later),

$$\begin{aligned}\mu(r,\tau) &= \sum_{ij}\mu_{ij}(r,\tau) \\ &= \sum_{ij} a_{ij}(r)\cos\big(2\pi\tau f_0 - \phi_{ij}(r)\big)e^{-\left(\tau-\tau_{ij}(r)\right)^2/2\Delta\tau^2}.\end{aligned} \tag{17}$$

Here, f_0 is the original central frequency of the equivalent Gaussian shaped ship-noise in the frequency domain and $\Delta f = 1/\Delta\tau$ is the bandwidth. In the case of RR03, $f_0 = 15$ Hz and $\Delta\tau = 0.05$ s were used and roughly correspond to the usable frequency band of 5–25 Hz.

To evaluate the TDOAs $\tau_{ij}(r)$ and the PDOA $\phi_{ij}(r)$ a ray-tracing propagation model was used (Jensen *et al.*, 2011). The sound speed profile used for the simulations was

statistically estimated thanks to the World Ocean Atlas for the winter season (Boyer *et al.*, 2018). The acoustic properties of the ocean bottom were approximated as a semi-infinite elastic medium of P-wave speed 2000 m/s and S-wave speed 500 m/s and allowed us to estimate roughly the PDOAs due to total reflection at different incidence angles.

To predict the strength of each interference, the following data-driven approach was chosen. Without any knowledge of the ocean floor acoustical properties, it is complicated to estimate with accuracy the amplitude of the different possible paths between the source (ship) and the receiver (OBS) and hence to predict the strength of the interferences. To build the propagative model, ten good quality ship passages were chosen during the calibration time period of November where high quality T-AIS data were available along with low biologic sound pollution. The cepstrogram of each passage was computed and time was converted into distance thanks to the accurate knowledge of the ship trajectories provided by the T-AIS data. This allowed us to align the different passages on the same distance scale. A statistical stacking was performed using the envelope of the cepstrogram [Fig. 5(a)] to avoid small phase misalignments (see Appendix C). For our test station RR03, three interferences are primarily observed (13, 35, and 57) up to 50 km distance and were hence modeled. The amplitude of those interferences were approximated by manually fitting asymmetric Gaussian functions (Azzalini and Capitanio, 1999) depending on the distance (see Appendix C).

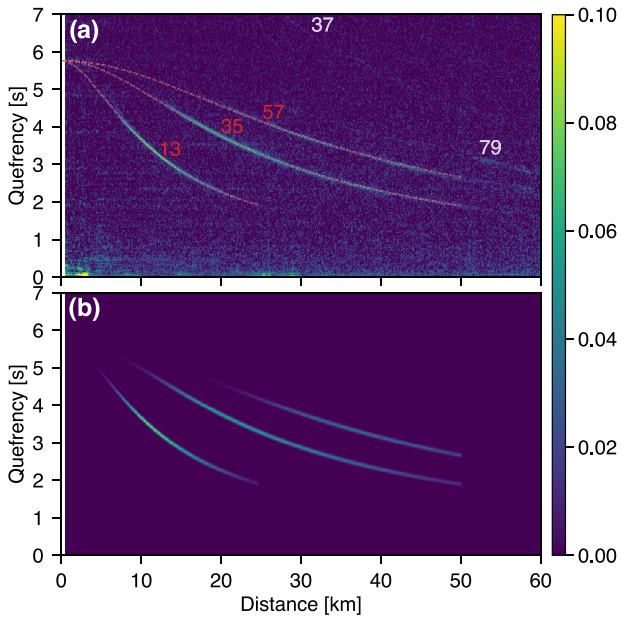

FIG. 5. (Color online) Cepstral model for the station RR03 as a function of the ship distance. (a) Observed cepstrogram envelope resulting from stacking ten good quality ship passages with well-known trajectories estimated from T-AIS data. Three interferences are clearly visible: 13, 35, and 57 (see also Fig. 4). Two more branches (37 and 79) can be guessed but are barely visible and will be neglected. Beyond 50 km between the source and the receiver, it will be considered that no interferences can be observed. Theoretical TDOAs computed by ray tracing match well the observed branches (dashed red lines). (b) Modeled cepstrogram envelope resulting from a hybrid approach where the TDOAs (and PDOAs) are estimated theoretically from the ray tracing computation and the amplitude is fitted from the data, here by asymmetric Gaussian functions.

Detection was performed on the same 3 min sliding windows used for the azimuthal estimation. Because of the high accuracy of cepstral analysis, the motion of the ship had to be considered. It was supposed that, on time scales of a few minutes, the radial ship motion can be well approximated by a constant radial speed model $r' = r + v\delta t$. This introduces a new variable v that can be constrained by the radial detector. For simplicity, it was considered that all values of the time-quefrency window were independent which gives the following computation for the likelihood ratio,

$$\mathcal{L}_r(y_r|t,r,v) = \prod_{|\delta t|<T/2} \prod_{\tau} \frac{\mathcal{N}\left(y_r(t,\tau)|\mu(r+v\delta t,\tau),\sigma^2(\tau)\right)}{\mathcal{N}\left(y_r(t,\tau)|0,\sigma^2(\tau)\right)}. \tag{18}$$

Computing the log likelihood ratio gives

$$\log \mathcal{L}_r(y_r|t,r,v) = \sum_{|\delta t|<T/2} \sum_{\tau} \frac{\mu(r+v\delta t,\tau)}{\sigma^2(\tau)} \left(y_r(t,\tau) - \frac{\mu(r+v\delta t,\tau)}{2} \right). \tag{19}$$

To decide if a ship is present, the following prior probability was used. It was supposed that the presence of a ship is *a priori* equiprobable with its absence. We supposed equiprobable any ship position and direction in the surveillance area. In polar coordinates, the infinitesimal surface at a given distance is proportional to the radius. This translates into a distance prior which is proportional to the distance over [0, 50] km. In the lack of knowledge of the ship speed, the prior on the radial speed was simply chosen to be uniform in the range [–25, 25] knots:

$$\mathcal{P}_r^-(t,r,v) = \begin{cases} \dfrac{2r}{r_{\max}^2} \dfrac{1}{(v_{\max}-v_{\min})}, & 0 \le r \le r_{\max}, -v_{\max} \le v \le v_{\max} \\ 0 & \text{otherwise.} \end{cases} \tag{20}$$

Limiting the grid search to a maximal speed helps to exclude improbable interference associations resulting from impossible ship speeds. The posterior probability was computed as

$$\mathcal{P}_r^+(t,\, r,\, v|y_r) = \mathcal{L}_r(y_r|t,\, r,\, v)\mathcal{P}_r^-(t,r,\, v). \tag{21}$$

The criterion of presence was computed by marginalizing on all possible states:

$$\mathcal{P}_r^+(t,\, \mathbb{1}|y_r) = \int_0^{r_{\max}} \int_{v_{\min}}^{v_{\max}} \mathcal{P}_r^+(t,\, r, v|y_r) dv dr. \tag{22}$$

Based on that criterion, the final radial detector can be defined:

https://doi.org/10.1121/10.0016810

$$\hat{r}(t), \hat{v}(t) = \begin{cases} \underset{r,v}{\operatorname{argmax}} \mathcal{P}_r^+(t, r, v|y_r), & \mathcal{P}_r^+(t, \mathbb{1}|y_r) > 1 \\ \varnothing & \text{otherwise.} \end{cases} \tag{23}$$

The marginalized log-likelihood ratio over speed for the test ship of November 27 calculated from the cepstrogram Fig. 6(a) is presented in Fig. 6(b) and the corresponding detections are shown in Fig. 6(c). The interference association problem can be observed as the presence of multiple possible distances. Nevertheless, at times when several branches can be observed, the log-likelihood ratio contributions sum on a unique distance of higher probability. It allows us to retrieve the ship distance up to 50 km. The association problem is partially solved as in most situations, the correct distance was recovered, except for some brief time periods. A small shadow-zone can be observed when the ship is closer than about 7 km from the OBS. At shorter distances, waves arrive with higher incidence angles and prevent total reflection (Kuperman and Roux, 2007) which highly reduce the interference phenomena.

D. Temporal segmentation

Simultaneous azimuthal and radial detections are required to determine the ship position at a given time.

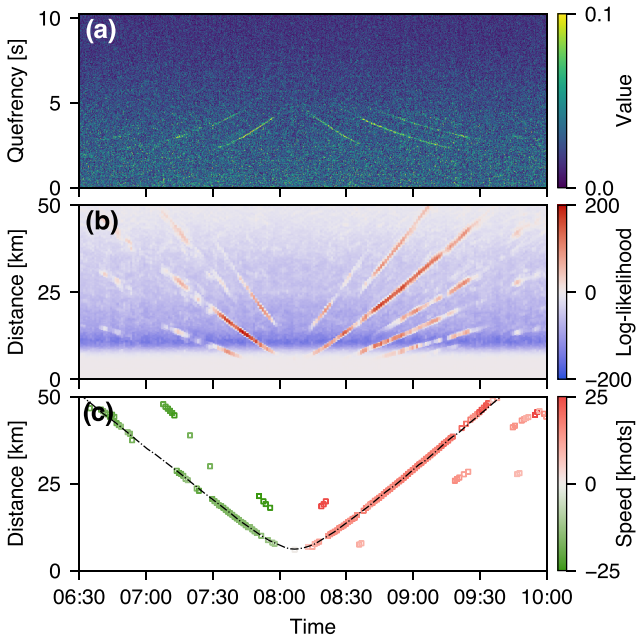

FIG. 6. (Color online) Range detection of the same ship passage at the same station than Fig. 3. (a) Cepstrogram, showing clearly the 13, 35, and 57 interference patterns (see also Fig. 4). (b) Using the cepstral model, the log-likelihood ratio is computed and marginalized along the speed dimension. It results in the presence of multiple branches, requiring solving the association problem. The locations where several hypothetical branches sum up have higher likelihood. (c) When the Bayes criterion is met, the range and the speed (color-coded from green to red, indicating approaching and leaving sources, respectively) are estimated at the maximum likelihood. In most cases, the right distance and speed is measured (the black dashed line indicates the AIS-derived distance curve of the ship relative to station RR03).

Because either can fail at some time steps, this results in a suboptimal approach with a reduced number of complete detections. Furthermore, the interference association problem is only partially solved by the radial detector. For those reasons, a different strategy trying to find continuity over a longer time period was chosen to reconstruct the ship path.

As mentioned earlier in this study, ships were hypothesized to travel rectilinearly at constant speed. This implies that any ship passage consists of a unique entry time in the monitored area, a unique approaching phase, a unique Closest Point of Approach (CPA), a unique leaving phase, and a unique exit time. As a result, it was chosen to first construct a meta-detector able to perform a temporal segmentation of the data associated with the presence of a unique ship, and then to find the optimal rectilinear track within that temporal window.

We decided to only consider cases where continuous detection could be performed for at least one hour. We defined the general probability ratio of the presence of a ship as the probability of continuous detection of a ship with both azimuthal and radial detectors during 1 h. To consider the fact that both detectors can miss some detections, a probability of detection was empirically attributed to each detector depending on their robustness ($P_\alpha^d = 90\%$ and $P_r^d = 60\%$). The probability of presence is then considered as the sum of two cases: the case when the ship is present and well detected and the case when the ship is present but not detected (for both detectors),

$$\mathcal{P}_g^+(t, \mathbb{1}|y) = \prod_{|\delta t|<T/2} \left(P_\alpha^d \mathcal{P}_r^+(t+\delta t, \mathbb{1}|y_r) + \left(1 - P_\alpha^d\right)\right) \times \left(P_r^d \mathcal{P}_r^+(t+\delta t, \mathbb{1}|y_r) + \left(1 - P_r^d\right)\right). \tag{24}$$

When multiple ships enter the detection zone at the same time, the algorithm may not be able to discriminate them. To split temporal segments containing several ships, two more meta-detectors are proposed: an approaching and a leaving detector that only consider the radial information by either marginalizing over the positive or the negative radial speeds

$$\mathcal{P}_{v\pm}^+(t, \mathbb{1}|y) = \prod_{|\delta t|<T/2} \left(P_r^d \mathcal{P}_{v\pm}^+(t+\delta t, \mathbb{1}|y_r) + \left(1 - P_r^d\right)\right). \tag{25}$$

Here, $\mathcal{P}_{v\pm}^+(t, \mathbb{1}|y)$ is computed as $\mathcal{P}_r^+(t, \mathbb{1}|y)$ in Eq. (22) but by only summing on positive/negative speeds v. An approaching/leaving detection is raised when at least one detector is triggered. In case both detectors are triggered, the one with the higher value decides if the target is approaching or leaving. Those three detectors (general, approaching, and leaving) result in three detection situations: general detection, approaching detection, and leaving detection. The general detector being more robust, it triggers the beginning and the end of each temporal segment of the presence of a unique ship. The approaching/leaving detectors are used to separate different ship paths by splitting temporal segments at the time when leaving phase is followed by an approaching phase (of another ship). This approach allowed us to

correctly segment the test week (Fig. 7) except for the very confused situation where three segments were retrieved whereas the sounds of four ships were overlapping at the same time in the first half of May 25, 2013.

E. Trajectory estimation

Once the temporal segmentation is performed, the final solution of the ship trajectory consists in finding the overall MAP ratio over the entire temporal segment $[t_s, t_e]$ (where t_s and t_e are respectively the start time and the end time of the segment). Four parameters must be optimized: the CPA time t_{CPA} and distance r_{CPA}, the ship heading α_∞ and speed v_∞. Let $p = (t_{CPA}, r_{CPA}, \alpha_\infty, v_\infty)$ be the track parameters. The posterior probability ratio of the track with parameter p is

$$\mathcal{P}^+(p|y) = \prod_{t\in[t_s,t_e]} \left(P_\alpha^d \mathcal{P}_\alpha^+(t,\alpha(t|p)|y_r) + \left(1-P_\alpha^d\right)\right) \times \left(P_r^d \mathcal{P}_r^+(t,r(t|p),v(t|p)|y_r) + \left(1-P_r^d\right)\right). \quad (26)$$

At this stage, the problem is simple enough to perform a brute force optimization by grid search. The obtained parameters fit well with the ground truth extracted from S-AIS data (Fig. 8). Branch association error occurred for only one ship passage, suggesting that imposing a continuous track is generally sufficient to solve this problem.

F. Performances

To evaluate and quantify the performances of the azimuthal and radial detectors along with the performance of the tracker, errors are computed by comparing results with the ground truth provided by the AIS dataset (Table I). Standard Median Absolute Deviation (SMAD) was used as a robust estimator of errors. Both the azimuthal and radial detectors allowed us to detect the ship very well, even in multi-source situations. The azimuthal detector shows greater completeness of detection than the radial detector, highlighted by the greater overall number of detection

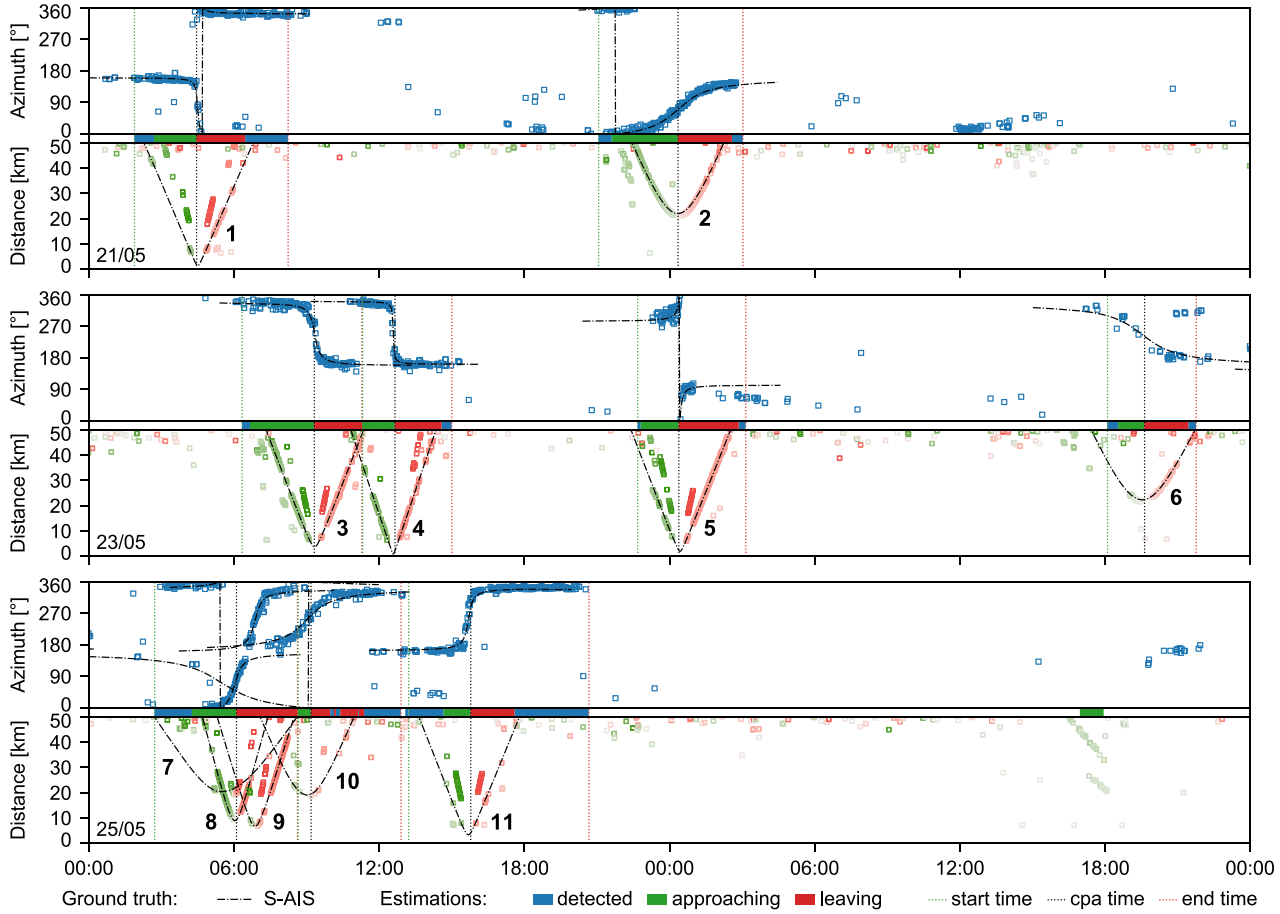

FIG. 7. (Color online) Detection and temporal segmentation over the six days test period from May 21 to 26, 2013, at seismic station RR03. The related spectrogram of the hydroacoustic component during these six days is presented Fig. 2. The upper part of the plots displays the azimuthal detections (blue squares) compared to the actual trajectories of the 11 ships obtained from the S-AIS (black dashed-dotted line and black numbers). The lower part displays the results of the radial detector (green to red squares, color coding speed according to the colormap used in Fig. 6(c). The two detectors show complementary features. The azimuthal detector seems robust and performs at a higher range while the radial detector seems very accurate but is limited to the 7–50 km range and can be very inaccurate due to the interference association problem. The central part of the plots displays the output of the meta-detectors. In the blue area, temporal duration is raised where there is a general ship detection. Periods in which an approaching/leaving phase is detected are in green and red. Based on this meta-detection, a temporal segmentation can be performed (vertical dotted lines). Note that coherent azimuthal and radial detections observed at the end of May 26 could be related to the presence of pigmy blue whales in the area (see also Fig. 2) emitting in the same frequency bands as the ones used here for ship detection and tracking, suggesting the ability of these detectors to be used for bio-acoustic sources.

https://doi.org/10.1121/10.0016810

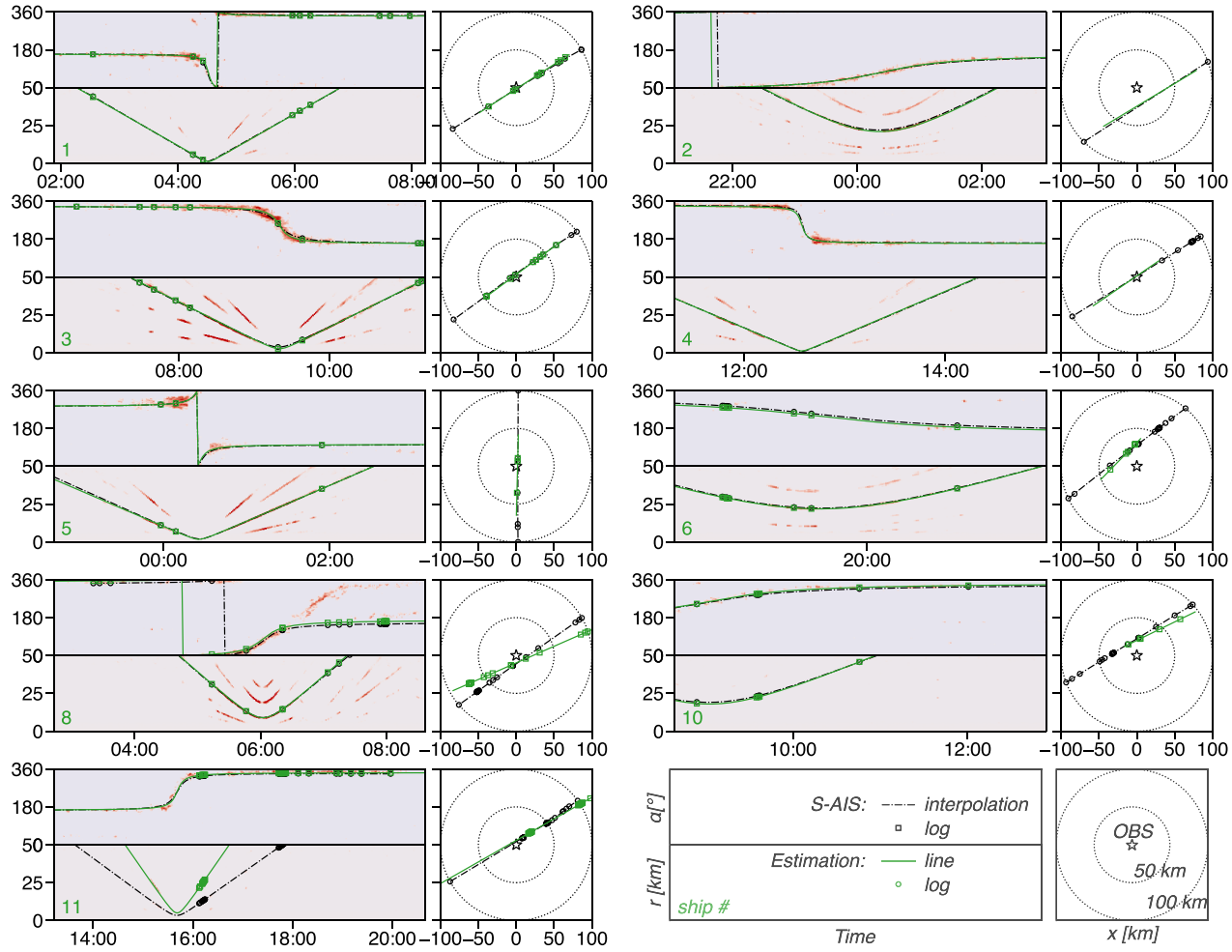

FIG. 8. (Color online) Ship tracking over the nine temporal segments detected (see Fig. 7). Each subplot is divided into three parts. The lower right subplot contains the legends and units of the subplots. For each detection, the upper left part corresponds to the azimuthal tracking while the lower left part corresponds to the radial tracking. For both, the log-likelihood ratio is displayed in the background with the same colormap used in Figs. 3(b) and 6(c). Note that in that case, the newly introduced probability of detection implies a minimal value which corresponds to the fact that no detection does not necessarily imply no ship. The diagram on the right part is a geographic map centered on the OBS location (star) with a circle at 50 and 100 km around it, showing the reconstruction of the ship trajectories. On the three diagrams, the retrieved trajectory indicated by green lines is compared to the true ship path, as provided by the S-AIS indicated by black dashed-dotted lines. Actual S-AIS ship positions are also shown (black squares and green circles) to better understand where the true ship position is best constrained.

(2004 vs 777) but a quite rough accuracy of 7.3°. The radial detector allowed overall great accuracies of about 500 m and 0.5 knots. Integrating over long time windows, the tracker raised improved results in terms of heading estimation (about 4°) and speed estimation (0.35 knots), and a CPA time estimate of about 1 min. The tracker did not allow us to improve the distance accuracy. This suggests that rectilinear trajectory assumption is not accurate enough to fit the real trajectory and becomes a limiting factor.

IV. CONCLUSION

We demonstrated in this paper that OBSs can be used as fully passive sonars to detect, localize and track ships in the open ocean. Two requirements are needed: the knowledge of the station orientation and localization, and a propagative model of the oceanic waves in the area. Using a small set of ship passage of known trajectories, a previous study (Trabattoni *et al.*, 2019) and the current study show that both can be estimated. The detection process relies on two independent detectors. First, we developed an azimuthal detector that estimates the direction of incoming hydroacoustic waves combining data from both the three-component seismometer and the co-located hydrophone. This detector achieved source azimuth accuracies of less than ten degrees at a range up to one hundred kilometers. Because the azimuthal detector is sensitive to the high and narrowband energy parts of the signal, it provides a robust and continuous monitoring of ships. Second, we developed a radial detector that relies on the analysis of the multipath interference patterns to estimate the distance and radial speed of ships. This detector achieves a distance accuracy of a few hundreds of meters, and a radial speed accuracy of few tenths of knots. It relies on the analysis of the less energetic wideband part of ship signals and is consequently limited to smaller detection range of about 50 km. It may be

TABLE I. Performances of the detectors and trackers computed over the six-day test period and the eleven vessels crossing the area, expressed by the mean of SMAD. Accuracies do not take into account false detections, possibly due to other sources not present in the S-AIS dataset, nor errors due to wrong interference association of the radial detector. The high number of azimuthal detections testify the robustness of this detector that uses the high intensity narrowband part of the ship noise. The radial detector uses the less energetic wideband part of ship noise hence is less robust but is very accurate. The tracker performance is evaluated by comparing the four parameters of the retrieved rectilinear trajectory with those of a fitted linearized version of the trajectory provided with the S-AIS dataset.

	Azimuthal detector		Radial detector			Tracker			
#	N	Heading (°)	N	Distance (m)	Speed (knots)	CPA time (s)	Heading (°)	CPA distance (m)	Speed (knots)
1	287	4.2	40	377	0.21	83	1.3	108	0.19
2	293	7.8	169	997	0.56	86	1.8	1031	0.13
3	251	9	135	315	0.48	33	0.8	1098	0.02
4	178	5.6	79	370	0.51	22	2.5	235	0.13
5	103	17	116	452	0.48	30	1.3	233	0.30
6	43	19.7	80	541	0.46	8	8.1	482	0.29
7	—	—	—	—	—	—	—	—	—
8	156	7.2	67	400	0.34	12	11.6	32	0.31
9	—	—	—	—	—	—	—	—	—
10	166	13.6	20	825	0.60	36	5.5	1112	0.53
11	283	7.3	15	446	0.68	9	2.6	1618	12.92
All	2004	7.3	777	526	0.48	45	3.6	531	0.35

also limited by potential misinterpretations of the interference branches that can lead to wrong results. Also, interferences are difficult to observe at low range (below 7 km), where the reflection on the ocean floor is limited. Combining both detectors into a continuous, completely autonomous tracker allows us to combine the strengths of both detectors. The tracker relies on the hypothesis that ship travels at constant heading and speed in high sea and assumes that at most one ship is present. Applied on a week of data of one single OBS, it allowed us to correctly retrieve the trajectory of most ships, except when multiple ships crossed the area at the same time. In perspective, generalizing the tracker to the case of multiple-source scenario, along with non rectilinear trajectories, should allow for the treatment of more complex situations. It is also expected that the approach proposed here could easily be transposed to detect and track marine mammals from ocean bottom fully passive observations. This work, emphasizing the single OBS detection and tracking capabilities, lays the foundation for future evolutions toward automatic surveillance of an area by a network of OBS and toward real-time analyses, as soon as the seismic networks will become cabled and able to deliver real-time data.

ACKNOWLEDGMENTS

RHUM-RUM (http://www.rhum-rum.net) was funded by ANR (Agence Nationale de la Recherche) in France (project ANR-11-BS56-0013), and by DFG (Deutsche Forschungsgemeinschaft) in Germany (Grant Nos. SI1538/2-1 and SI1538/4-1). We thank DEPAS (Deutsche Geräte-Pool für Amphibische Seismologie, Germany), GEOMAR (GEOMAR Helmholtz-Zentrum für Ozeanforschung Kiel, Germany), and INSU-IPGP (Institut National des Sciences de l'Univers – Institut de Physique du Globe de Paris, France) for providing the ocean-bottom seismometers. The RHUM-RUM dataset (http://dx.doi.org/10.15778/RESIF.YV2011) has been assigned the FDSN network code YV and is hosted and served by the French RESIF data centre (http://seismology.resif.fr). Codes used to explore OBS datasets and to detect and track ships are available in a package named *obsea*, available at https://github.com/atrabattoni/obsea. Codes used to produce the figures of this article can be found at https://github.com/atrabattoni/tracking_ships_with_obs. The author's PhD was funded by the STEP'UP doctoral school of *Université de Paris* and by the French *Direction Générale de l'Armement* (DGA).

APPENDIX A: CEPSTROGRAM DECOMPOSITION INTO SOURCE AND PROPAGATION TERM USING SVD

A received signal $x(t)$ can be written as the convolution of a source term $s(t)$ and a propagation term $g(t)$: $x(t) = s(t) * g(t)$. Using the convolution theorem, the spectrogram of this signal can be written as: $|S_x(t,f)|^2 = |S_s(t,f)|^2 |S_g(t,f)|^2$. Taking the logarithm, we get the log spectrogram as $\log|S_x(t,f)|^2 = \log|S_s(t,f)|^2 + \log|S_g(t,f)|^2$. As a consequence of the linearity of the (inverse) Fourier transform, the cepstogram can be written as the sum of a source and a propagation term: $C_X(t,\tau) = C_S(t,\tau) + C_G(t,\tau)$. In the case of a repetitive moving source the fact that the source term is time-invariant whereas the propagative term evolves through time allows us to use SVD filtering (Demene *et al.*, 2015) to perform the decomposition. The time-averaged cepstrum is subtracted from the whole cepstrogram and SVD is applied. The SVD summarizes the cepstrogram into a sum of unitary time-invariant cepstrums (the singular vectors) associated with the quantity of signal they represent (the singular values). The way the energy is spread among the time-invariant singular vectors is related to the

https://doi.org/10.1121/10.0016810

time-invariant aspect of the signal. The most energetic singular vectors, mainly containing the source term, can be separated from the remaining singular vectors containing the propagation term (and noise). The separation of the singular values is automatically chosen using the kneedle algorithm (Satopaa *et al.*, 2011). To obtain the propagative term, source-related singular values are set to zero. More details can be found in Trabattoni *et al.* (2019).

APPENDIX B: CHOICE OF STATISTICAL DISTRIBUTIONS

To support the choice of the Wrapped-Cauchy and Normal distributions to represent, respectively, the azimuthal and the cepstral data, Monte Carlo simulations were performed. In both cases, a long stationary signal is generated and processed, and statistics are computed on the different time-bins available.

Considering a Gaussian source located at some azimuth of the sensors, the expected horizontal velocities can be estimated by geometric projection. The pressure is simply proportional to the source. Using Eq. (5), the azimuth can be estimated. To measure the corruption implied by ambient noise uncorrelated Gaussian noises were added at different SNR [see SNR = 40 dB in Fig. 9(a)]. It appears that at high SNR the azimuthal data can be modeled by a Wrapped

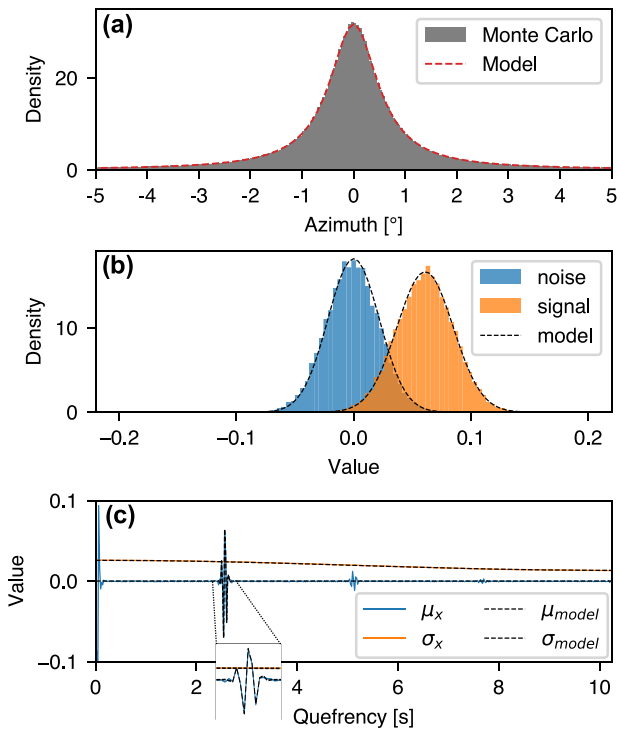

FIG. 9. (Color online) Validation of the statistical models by Monte Carlo simulation. (a) At high SNR, a Gaussian source corrupted by isotropic Gaussian noise follows a Wrapped-Cauchy distribution with circular variance inversely proportional with the square root of the SNR. (b) Every bin of the cepstrogram follows a normal law whose variance and mean mainly depends on the quefrency and the state of the ship. (c) The variance of cepstrogram only depends on the quefrency. The mean is mainly null except at the quefrency where multipath interference occurs. Both parameters can be accurately modeled.

Cauchy process in which circular variance $1-R$ is equal to $1/\sqrt{\text{SNR}}$. Because the Fourier transform of Gaussian white noise is also a Gaussian white noise, each frequency "channels" of the STFT turned out to show the same results.

The wideband part of ship noise can be considered as a colored Gaussian source. It is modeled by the convolution of a zero-mean, unit-variance white Gaussian source with a unit-amplitude Gaussian pulse of central frequency 15 Hz and bandwidth 5–25 Hz (at −6 dB). As the multipath information is carried by the wideband part of ship noise and because SVD filtering has the effects of removing the harmonic structure of ship noise this latter was not modeled. The multipath propagation was modeled by convolution of a time function with unit value at the origin time and 0.5 value at 2.56 s (128 samples at 50 Hz). The ambient noise was modeled as zero-mean, unit-variance white Gaussian noise giving a SNR close to one. The cepstrogram can be estimated with Eq. (14) with the same parameters. Computing statistics on different time bins of the cepstrogram for this stationary signal exhibits several features. The bins of the cepstrogram follow normal laws [Figs. 9(b) and 9(c)]. The variance of the normal laws only depends on the quefrency following Eq. (15). The mean depends on the presence and distance of the ship according to Eq. (17). We can observe the presence of some rahmonics (harmonics in the quefrency domain) at multiples of the TDOA that are due to the nonlinearity of the cepstral analysis (due to the use of the log function). The importance of those rahmonics is linked to amplitude ratio at the power of the rahmonic number (due to the Taylor expansion of the log) between the direct arrival and the echo. In general, those rahmonics are below the noise level. The shape of the resulting pulse in the quefrency domain [see inset in Fig. 9(c)] is linked to the bandwidth where ship noise dominates in the frequency domain. It is very close to the model for SNR = 1. At lower SNR it vanishes toward zero. At higher SNR it tends toward a Dirac pulse.

APPENDIX C: STATISTICAL STACKING OF THE CEPSTRUM ENVELOPE

It is assumed that the different values of the cepstrum $C_x(\tau)$ for the different quefrencies τ follow normal laws of means $\mu(\tau)$ and variances $\sigma^2(\tau)$. The cepstrum can be written into its analytical representation as $\hat{C}_x(\tau) = C_x(\tau) + iC_x^H(\tau)$ (the H superscript standing for Hilbert Transform). Here, values of $C_x^H(\tau)$ also follow normal laws of the same variances but different means $\mu_H(\tau)$. The complex mean of the values $\hat{C}_x(\tau)$ is $\hat{\mu}(\tau) = \mu(\tau) + i\mu_H(\tau)$. The goal is to estimate the mean of the envelope $|\hat{\mu}(\tau)|$. The square of the envelope normalized by the variance is the sum of the square of two normally distributed variables with unit variance that by definition follows a noncentral χ^2 law with $k = 2$ degrees of freedom and non-centrality parameter $\lambda(\tau) = \mu^2(\tau) + \mu_H^2(\tau) = |\hat{\mu}(\tau)|^2$,

$$\left|\frac{\hat{C}_x(\tau)}{\sigma(\tau)}\right|^2 = \left|\frac{C_x(\tau)}{\sigma(\tau)}\right|^2 + \left|\frac{C_x^H(\tau)}{\sigma(\tau)}\right|^2 \sim \text{noncentral}\,\chi^2(k, \lambda(\tau)). \quad \text{(C1)}$$

Because the mean of this statistical law is $k + \lambda$, the mean of the envelope can be estimated by

$$|\hat{\mu}(\tau)| = \sigma\sqrt{E\left[\left|\frac{\hat{C}_x(\tau)}{\sigma(\tau)}\right|^2\right] - k}, \quad \text{(C2)}$$

where $E[\cdot]$ denotes the expected value on different realizations that in the study case corresponds to the different ship passages.

APPENDIX D: ASYMMETRIC GAUSSIAN FUNCTION FITTING

The strengths $\mu_{ij}(r)$ of the interference between the path i and path j in function of the distance r was approximated by fitting asymmetric Gaussian functions (Azzalini and Capitanio, 1999). The fitting was done onto the average observed envelope of the cepstrogram [see Fig. 5(a) and Appendix A]. The motivation for this type of function was purely subjective and allowed us to fit the observation (Fig. 10). The asymmetric Gaussian function $f(x)$ also known as the Probability Density Function (PDF) of the skew normal distribution is defined as

$$f(x) = 2\phi(x)\Phi(\alpha x), \quad \text{(D1)}$$

where $\phi(x)$ and $\Phi(x)$ are, respectively, the PDF and the Cumulative Distribution Function (CDF) of the standard normal distribution, while α is the shape parameter that allows us to specify the asymmetry of the function. To add the location ξ and scale ω parameters, the transform $x \rightarrow (x - \xi)/\omega$ was used. An amplitude scaling k was also used.

Values along the theoretical TDOA [red dashed line in Fig. 5(a)] were extracted for each interference at each distance and then manually fitted. Obtained parameters are summarized in Table II.

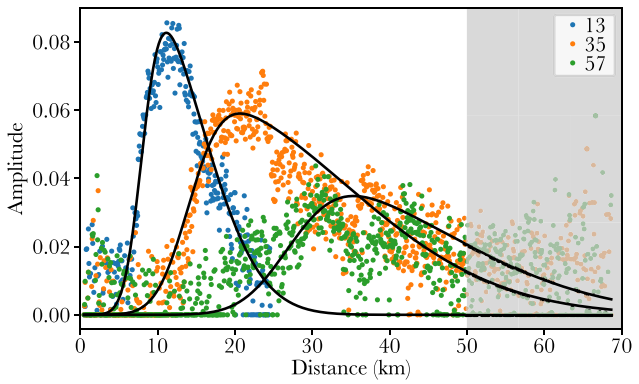

FIG. 10. (Color online) Manual asymmetric Gaussian fitting of the cepstrum envelope [Fig. 5(a)] to complete the cepstral modeling [Fig. 5(b)]. Values for each interference (colored circles) were extracted from Fig. 5(a) along the line given by the TDOA model. The fit provides the expected strengths of each interference 13, 35, and 57 in the function of the distance (black lines). Values above 50 km were not taken into account as interferences were assumed to be unobservable beyond that distance.

TABLE II. Asymmetric Gaussian parametrization manually fitted on the observed cepstrogram [Fig. 5(a)] envelope to complete the statistical modeling of the ceptrogram [Fig. 5(b)].

Interference	k	α	ξ (km)	ω (km)
13	$8{,}9.10^2$	4,0	8,0	7,5
35	$1{,}6.10^3$	6,0	14,0	20,0
57	$1{,}0.10^3$	4,0	27,0	20,0

Azzalini, A., and Capitanio, A. (**1999**). "Statistical applications of the multivariate skew normal distribution," J. R. Statistical Soc. B **61**, 579–602.

Barruol, G., and Sigloch, K. (**2013**). "Investigating La Réunion hot spot from crust to core," Eos. Trans. AGU. **94**, 205–207.

Barruol, G., Sigloch, K., Scholz, J.-R., Mazzullo, A., Stutzmann, E., Montagner, J.-P., Kiselev, S., Fontaine, F. R., Michon, L., Deplus, C., and Dyment, J. (**2019**). "Large-scale flow of Indian Ocean asthenosphere driven by Réunion plume," Nat. Geosci. **12**, 1043–1049.

Bouffaut, L., Dréo, R., Labat, V., Boudraa, A.-O., and Barruol, G. (**2018**). "Passive stochastic matched filter for Antarctic blue whale call detection," J. Acoust. Soc. Am. **144**, 955–965.

Boyer, T. P., García, H. E., Locarnini, R. A., Zweng, M. M., Mishonov, A. V., Reagan, J. R., Weathers, K. A., Baranova, O. K., Paver, C. R., Seidov, D., and Smolyar, I. V. (**2018**). "World Ocean Atlas 2018 [Temperature and Salinity]," NOAA National Centers for Environmental Information, Dataset, https://www.ncei.noaa.gov/archive/accession/NCEI-WOA18 (Last viewed 1/12/2022).

Demene, C., Deffieux, T., Pernot, M., Osmanski, B.-F., Biran, V., Gennisson, J.-L., Sieu, L.-A., Bergel, A., Franqui, S., Correas, J.-M., Cohen, I., Baud, O., and Tanter, M. (**2015**). "Spatiotemporal clutter filtering of ultrafast ultrasound data highly increases Doppler and fUltrasound sensitivity," IEEE Trans. Med. Imag. **34**, 2271–2285.

Dréo, R., Bouffaut, L., Leroy, E., Barruol, G., and Samaran, F. (**2019**). "Baleen whale distribution and seasonal occurrence revealed by an ocean bottom seismometer network in the Western Indian Ocean," Deep Sea Res. Part II: Topical Stud. Oceanogr. **161**, 132–144.

Dréo, R., Trabattoni, A., Stinco, P., Micheli, M., and Tesei, A. (**2022**). "Detection and localization of multiple ships using acoustic vector sensors on buoyancy gliders: Practical design considerations and experimental verifications," IEEE J. Oceanic Eng. **1**, 1–15.

Essing, D., Schlindwein, V., Schmidt-Aursch, M. C., Hadziioannou, C., and Stähler, S. C. (**2021**). "Characteristics of current-induced harmonic tremor signals in ocean-bottom seismometer records," Seismolog. Res. Lett. **92**, 3100–3112.

FAO (**2020**). *The State of World Fisheries and Aquaculture 2020* (FAO, Quebec, Canada).

Ferguson, E. L., Williams, S. B., and Jin, C. T. (**2018**). "Sound source localization in a multipath environment using convolutional neural networks," in *Proceedings of the 2018 IEEE International Conference on Acoustics, Speech and Signal Processing (ICASSP)*, April 15–20, Calgary, Canada, pp. 2386–2390.

Fontaine, F. R., Barruol, G., Kennett, BL. N., Bokelmann, G. H. R., and Reymond, D. (**2009**). "Upper mantle anisotropy beneath Australia and Tahiti from P wave polarization: Implications for real-time earthquake location," J. Geophys. Res. **114**, B03306, https://doi.org/10.1029/2008JB005709.

Gao, L., Xia, J., and Pan, Y. (**2014**). "Misidentification caused by leaky surface wave in high-frequency surface wave method," Geophys. J. Int. **199**, 1452–1462.

Gervaise, C., Kinda, B. G., Bonnel, J., Stéphan, Y., and Vallez, S. (**2012**). "Passive geoacoustic inversion with a single hydrophone using broadband ship noise," J. Acoust. Soc. Am. **131**, 1999–2010.

Hable, S., Sigloch, K., Stutzmann, E., Kiselev, S., and Barruol, G. (**2019**). "Tomography of crust and lithosphere in the western Indian Ocean from noise cross-correlations of land and ocean bottom seismometers," Geophys. J. Int. **219**, 924–944.

Harris, D., Matias, L., Thomas, L., Harwood, J., and Geissler, W. H. (**2013**). "Applying distance sampling to fin whale calls recorded by single seismic instruments in the northeast Atlantic," J. Acoust. Soc. Am. **134**, 3522–3535.

Jensen, F. B., Kuperman, W. A., Porter, M. B., and Schmidt, H. (**2011**). *Computational Ocean Acoustics* (Springer, New York).
Kuperman, W., and Roux, P. (**2007**). "Underwater acoustics," in *Springer Handbook of Acoustics*, edited by T. D. Rossing (Springer New York, New York), pp. 149–204.
Mann, J. A., Tichy, J., and Romano, A. J. (**1987**). "Instantaneous and time-averaged energy transfer in acoustic fields," J. Acoust. Soc. Am. **82**, 17–30.
Mardia, K. V., and Jupp, P. E. (**1999**). *Directional Statistics, Wiley Series in Probability and Statistics* (John Wiley & Sons, Inc., Hoboken, NJ).
Mazzullo, A., Stutzmann, E., Montagner, J.-P., Kiselev, S., Maurya, S., Barruol, G., and Sigloch, K. (**2017**). "Anisotropic tomography around La Réunion Island from Rayleigh waves: Tomography of western Indian Ocean," J. Geophys. Res. Solid Earth **122**, 9132–9148, https://doi.org/10.1002/2017JB014354.
Oppenheim, A. V., and Schafer, R. W. (**2004**). "DSP history—From frequency to quefrency: A history of the cepstrum," IEEE Signal Process. Mag. **21**, 95–106.
Poor, H. V. (**1994**). "An introduction to signal detection and estimation," in *Springer Texts in Electrical Engineering* (Springer, New York).
Rako-Gospić, N., and Picciulin, M. (**2019**). "Underwater noise: Sources and effects on marine life," in *World Seas: An Environmental Evaluation* (Elsevier, Amsterdam), pp. 367–389.
Ritter, F., and Panigada, S. (**2019**). "Collisions of vessels with cetaceans—the underestimated threat," in *World Seas: An Environmental Evaluation* (Elsevier, Amsterdam), pp. 531–547.
Samaran, F., Stafford, K. M., Branch, T. A., Gedamke, J., Royer, J.-Y., Dziak, R. P., and Guinet, C. (**2013**). "Seasonal and geographic variation of southern blue whale subspecies in the Indian Ocean," PLoS One **8**, e71561.
Satopaa, V., Albrecht, J., Irwin, D., and Raghavan, B. (**2011**). "Finding a 'kneedle' in a haystack: Detecting knee points in system behavior," in *Proceedings of the 2011 31st International Conference on Distributed Computing Systems Workshops*, June 20–24, Minneapolis, MN, pp. 166–171.
Scholz, J.-R., Barruol, G., Fontaine, F. R., Mazzullo, A., Montagner, J.-P., Stutzmann, E., Michon, L., and Sigloch, K. (**2018**). "SKS splitting in the Western Indian Ocean from land and seafloor seismometers: Plume, plate and ridge signatures," Earth Planet. Sci. Lett. **498**, 169–184.
Stähler, S. C., Schmidt-Aursch, M. C., Hein, G., and Mars, R. (**2018**). "A self-noise model for the German DEPAS OBS pool," Seismolog. Res. Lett. **89**, 1838–1845.
Stähler, S. C., Sigloch, K., Hosseini, K., Crawford, W. C., Barruol, G., Schmidt-Aursch, M. C., Tsekhmistrenko, M., Scholz, J.-R., Mazzullo, A., and Deen, M. (**2016**). "Performance report of the RHUM-RUM ocean bottom seismometer network around La Réunion, western Indian Ocean," Adv. Geosci. **41**, 43–63.
Stinco, P., Tesei, A., Dreo, R., and Micheli, M. (**2021a**). "Detection of envelope modulation and direction of arrival estimation of multiple noise sources with an acoustic vector sensor," J. Acoust. Soc. Am. **149**, 1596–1608.
Stinco, P., Tesei, A., Ferri, G., Biagini, S., Micheli, M., Garau, B., LePage, K. D., Troiano, L., Grati, A., and Guerrini, P. (**2021b**). "Passive acoustic signal processing at low frequency with a 3-D acoustic vector sensor hosted on a buoyancy glider," IEEE J. Oceanic Eng. **46**, 283–293.
Stone, L. D., Streit, R. L., Corwin, T. L., and Bell, K. L. (**2014**). *Bayesian Multiple Target Tracking*, 2nd ed. (Artech House, Boston, MA), p. 293.
Thode, A. M., Sakai, T., Michalec, J., Rankin, S., Soldevilla, M. S., Martin, B., and Kim, K. H. (**2019**). "Displaying bioacoustic directional information from sonobuoys using 'azigrams,' " J. Acoust. Soc. Am. **146**, 95–102.
Trabattoni, A., Barruol, G., Dreo, R., Boudraa, A. O., and Fontaine, F. R. (**2019**). "Orienting and locating ocean-bottom seismometers from ship noise analysis," Geophys. J. Int. **220**, 1774–1790.
Tsekhmistrenko, M., Sigloch, K., Hosseini, K., and Barruol, G. (**2021**). "A tree of Indo-African mantle plumes imaged by seismic tomography," Nat. Geosci. **14**, 612–619.
Weirathmueller, M. J., Wilcock, W. S. D., and Hilmo, R. S. (**2017**). "Estimating range to a vocalizing fin whale using the timing and amplitude of multipath arrivals," J. Acoust. Soc. Am. **142**, 2101–2120.
Wilcock, W. S. D. (**2012**). "Tracking fin whales in the northeast Pacific Ocean with a seafloor seismic network," J. Acoust. Soc. Am. **132**, 2408–2419.
Wilcock, W. S. D., and Hilmo, R. S. (**2021**). "A method for tracking blue whales (*Balaenoptera musculus*) with a widely spaced network of ocean bottom seismometers," PLoS One **16**, e0260273.
Zhang, B., Matchinski, E. J., Chen, B., Ye, X., Jing, L., and Lee, K. (**2019**). "Marine oil spills—oil pollution, sources and effects," in *World Seas: An Environmental Evaluation* (Elsevier, Amsterdam), pp. 391–406.